Numerical modeling of perforated plates in oscillating flow

Fredrik Mentzoni*, Trygve Kristiansen

Department of Marine Technology
Norwegian University of Science and Technology
NO-7491 Trondheim, Norway

Abstract

Perforated plates, relevant for several marine applications, are experimentally and numerically investigated. The numerical investigations are performed using a presently developed Navier–Stokes solver. Several comparison and sensitivity studies are presented, in order to validate and verify the solver. Forced heave experiments are performed on two perforated plates with perforation ratios 19 % and 28 %. Amplitude-dependent added mass and damping coefficients are presented. Good agreement is obtained between the solver and the present experiments. Consistent with existing data, the results show that the hydrodynamic coefficients of perforated plates are highly amplitude dependent. The damping force is found to dominate over added mass force. The damping force dominance increases with increasing perforation ratio. It is highlighted that plate-end flow separation has an important effect on the damping coefficient. The developed numerical solver is two-dimensional, but is found to yield reasonable estimates of hydrodynamic force coefficients

---

☆Postprint of https://doi.org/10.1016/j.apor.2018.12.016

*Corresponding author
Email address: `fredrik.mentzoni@ntnu.no` (Fredrik Mentzoni)

when compared with a previous three-dimensional experimental investigation. This could indicate that three-dimensional effects are not dominant for the hydrodynamic forces of perforated plates, and that a two-dimensional viscous flow solver could have relevance as a tool for estimating hydrodynamic forces on three-dimensional perforated structures.

Keywords: Perforated plate, Numerical model, Damping, Added mass, Computational fluid dynamics, Experimental study

1. Introduction

The hydrodynamic behavior of perforated plates are relevant in several marine applications. Direct similarities exist between perforated plates and the ventilated or perforated structures that can be used to damp motions of structures, e.g. heave plates, swash bulkheads and wave absorbers, or are used in complex subsea structures, e.g hatch covers, mudmats and various protection structures. Complex subsea modules may also consist of rows of several densely packed equipment and pipes, for which the flow, and resulting loads, may be simplified to that of a perforated structure.

The motivation for this work is to reduce uncertainty when performing marine deployment operations, which is likely to be cost saving by reducing conservatism and delays when it comes to the time used on waiting for acceptable weather conditions. The objective of the project involves increased knowledge on the hydrodynamic loads on typical members of subsea structures, including how to account for interaction and shielding effects between different member types. In an initial study [1], experimentally obtained added mass and damping coefficients for different configurations of perforated plates and cylinders were presented. The challenges with estimating the hydrodynamic coefficients were highlighted. In the present study, further experimental investigations have been performed, as well as development of a numerical viscous flow solver, which can estimate hydrodynamic coefficients of these type of structures. The focus is how to model and compute coefficients for perforated plates. Special attention is given to the effect of flow separation at the plate-ends, which has been pointed out by several previous studies to be of importance [2, 3, 4, 5, 6].

Due to the industrial relevance, there has been a great deal of analytical, numerical and experimental investigations on perforated plates. Molin presented an extensive review in 2011 [6]. After his review paper, there has been other relevant studies, including the works by An and Faltinsen [2, 7], Li et al. [5], and Tian et al. [8], which will be briefly summarized in the following.

An and Faltinsen [7] studied semi-analytical solutions for two-dimensional perforated plates in infinite and finite water depths, and followed up with a three-dimensional study including an experimental investigation of two rectangular plates with perforation ratios of $8\,\%$ and $16\,\%$ [2]. Their semi-analytical investigation is based on using a vortex distribution along the plate, and their study includes both linear and quadratic pressure-drop conditions, the latter analysis yielding hydrodynamic coefficients corresponding to the result by Molin [6, 7]. In their experimental study, the two perforated plates, both with cross-sectional areas of $520\,\mathrm{mm} \times 365\,\mathrm{mm}$, were forced to oscillate at two different submergences, for different periods of motions and a range of amplitudes corresponding to Keulegan–Carpenter numbers,

$$\mathrm{KC} = \frac{WT}{D}, \tag{1}$$

with W the velocity amplitude, T the period of oscillation and D the characteristic width of the plate, of $0.17 \leq \mathrm{KC} \leq 1.7$ with KC based on the smallest of the two plate sides ($D = 365\,\mathrm{mm}$). They found strong amplitude dependence for both the added mass and damping coefficients. Improved agreement was found in the hydrodynamic coefficients between their experimental investigation and semi-analytical method when adding a drag force in order to account for flow separation at the plate-ends in an empirical manner.

Li et al. [5] performed an experimental study of heave plates for spar platforms. The plates were flat square sections of $400\,\mathrm{mm} \times 400\,\mathrm{mm}$ in size. Four of the tested plates were perforated, with perforation ratios of $1\,\%$, $5\,\%$ with two different hole sizes, and $10\,\%$. The plates were forced to oscillate harmonically in heave for Keulegan–Carpenter numbers ranging from $0.2 \leq \mathrm{KC} \leq 1.2$. The resulting added mass and damping coefficients were found to depend on the amplitude. It was pointed out that the differences in the (quadratic) damping coefficients between the three different perforation ratios becomes negligible for $\mathrm{KC} > 1.0$, and are similar to that of a solid plate. Only minor differences were found in both hydrodynamic coefficients between the two hole sizes tested.

Tian et al. [8] performed an experimental investigation of oscillating flat circular disks. Unlike many previous studies, their experiments included high KC numbers, with a total range $0.15 \leq \mathrm{KC} \leq 3.15$ when normalizing with the disk diameter. Seven perforated disks were investigated, with perforation ratios τ of, $\tau = 0.05$, $\tau = 0.10$ (five different hole sizes), and $\tau = 0.20$.

Amplitude dependence was found to be important for both the added mass and damping coefficients, for all perforation ratios, generally with increasing coefficients at increasing amplitude. A considerable decrease in the added mass coefficients was found when increasing the perforation ratio, with 40 %-60 % reduction of the most perforated disk ($\tau = 0.20$) compared to tests with a solid disk. The damping coefficients were less sensitive to the perforation ratio, with less clear trends when increasing the perforation ratio, however a slight reduction was in general found. The sensitivity to hole size was found to be small, and the coefficients were almost identical for the five different versions of the $\tau = 0.10$ disk, throughout the whole range of KC numbers tested.

The present study consists of four main parts. This introduction and the description of the experimental setup and potential flow methods serve as background (Sections 2-3). In the second part, the presently developed CFD method is described (Section 4). It is a basic, two-dimensional Navier–Stokes solver. Sensitivity studies and verification of the code are given. In the third part, the experimental results for two perforated plates are presented, and good agreement with the numerical counterparts of the CFD simulations is in general demonstrated (Sections 5.1-5.2). We conclude from this that the CFD is able to predict the main physical effects of the problem; i.e. the flow through and around the plates. In the fourth and last part, Section 5.3, we investigate differences between 2D and 3D plates.

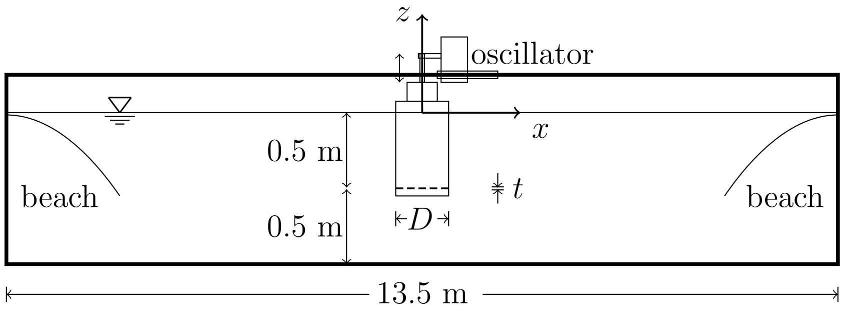

Figure 1: Principle sketch of the experimental setup in the present experiments carried out in a glass flume with dimensions $13.5 \times 1.0 \times 0.6\,\mathrm{m}$ at the Marine Technology center (see [1] for a more detailed description). Plate dimensions: $D = 420\,\mathrm{mm}$, $t = 3\,\mathrm{mm}$.

2. Experimental investigation

The present experimental investigations are based on the same setup and facilities as [1], except for the change of force transducer (6 kN compared to the previous 400 N). A sketch of the experimental setup is presented in Fig. 1. Forced oscillation tests are performed. The amplitudes of oscillation range from $Z = 1.7\,\mathrm{cm}$ to $Z = 13\,\mathrm{cm}$. The markers in the result figures are used to indicate the five different periods of oscillation tested: 1.0 s (diamonds), 1.25 s (pentagons), 1.5 s (hexagons), 1.75 s (circles), and 2.0 s (stars).

Two perforated plates, denoted P19 and P28, are tested. A picture of P28 placed in the experimental rig is presented in Fig. 2. The perforated plates consist of many small circular holes with sharp corners, making up perforation ratios of $\tau = 0.19$ and $\tau = 0.28$ for, respectively, P19 and P28, when accounting for two stiffeners used on the plates, as well as the profiles used to fasten the plates. The profiles and stiffeners are visible in Fig. 2. The thickness of the plates is $t = 3\,\mathrm{mm}$, while the lateral dimension (into the

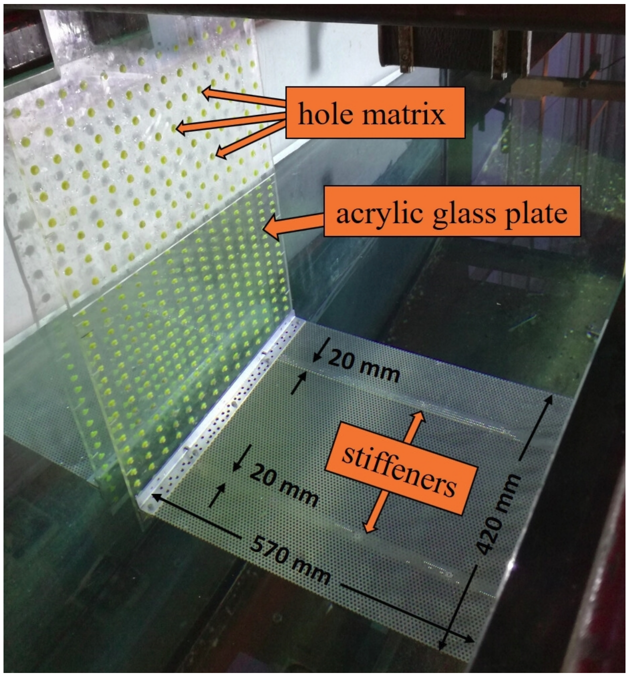

Figure 2: A photo of the perforated plate model denoted P28 (perforation ratio $\tau = 0.28$) placed inside the experimental rig (near bird's eye view). The acrylic glass plates with the hole matrix are indicated.

paper in Fig. 1) is $L = 570\,\mathrm{mm}$. More details are given in Table 1.

The perforated plates are fastened with screws through acrylic glass plates on each side, cf. Fig 2. The acrylic glass plates consist of a range of holes, making up a hole matrix which enables the possibility of testing several structures at different positions and submergences in the tank. The flexibility of the hole matrix was utilized in previous experimental investigations of simplified subsea structures [1]. Holes that are not used are filled with yellow putty to ensure a smooth surface on the acrylic glass plates.

The experimental, analytical and numerical results are presented in terms

Table 1: Characteristics of the two presently experimentally tested perforated plate models.

	Perforation ratio	Dry mass	Hole diameter	Material
P19	$\tau = 0.19$	2.3 kg	2 mm	5754 aluminum
P28	$\tau = 0.28$	2.1 kg	3 mm	5754 aluminum

of hydrodynamic coefficients. The coefficients are made nondimensional by the analytical added mass of a solid plate with the same area as the perforated plates tested,

$$A_0 = \frac{\pi}{4}\rho D^2 L, \tag{2}$$

with ρ being the density of the fluid. The nondimensional added mass coefficient is expressed as $\frac{A}{A_0}$. A linear damping model is used, and the nondimensional damping coefficient is expressed as $\frac{B}{\omega A_0}$, with ω being the circular frequency of motion. The motions are harmonically varying. Consequently, the added mass and damping are obtained by Fourier averaging.

The tested perforated plates are close to ideal, in the sense that they consist of many small holes (P19 with 2 mm hole diameter: $\approx 15\,000$, P28 with 3 mm hole diameter: $\approx 10\,000$), and thus would yield negligible added masses in the low-KC limit. Note that the two stiffeners used on the plates are non-perforated and cover approximately 9 % of the total area of the plates, hence some added mass in the low-KC limit should be expected. The effect of the stiffeners was calculated to yield $\frac{A}{A_0} \approx 0.02$ by using the source panel method [1].

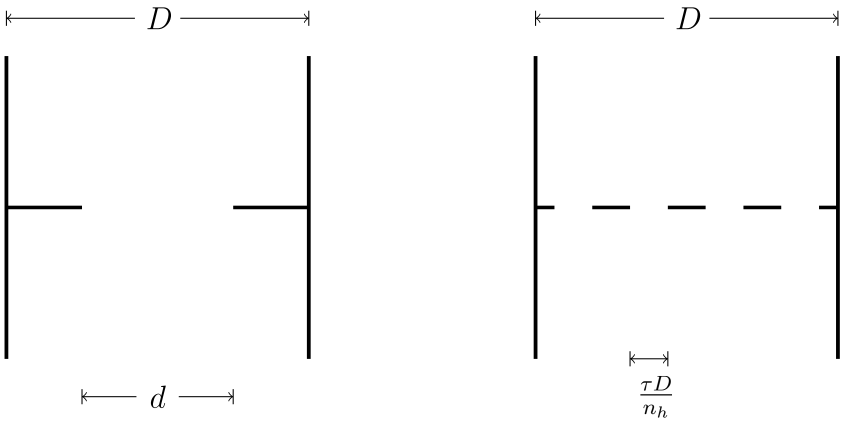

Figure 3: Parameters involved in the numerical investigations of flow through one opening in a channel (left) and several openings in a channel (right).

3. Potential flow methods

Two potential flow methods are presented in the following. First, an analytical method is described (Section 3.1). This method estimates the added mass of a perforated plate for KC → 0 by modeling the flow through the openings of the plate as the flow through openings in a channel. Second, a source panel method, which can provide added mass coefficients for KC → 0 in both open and channel flow conditions, is presented (Section 3.2). Later in the text, we compare results obtained by these methods with the experimental investigations and numerical viscous flow solver, in order to increase our understanding of, and confidence in, the results.

3.1. Analytical added mass for flow through openings in a channel

The analytical result for the added mass due to potential flow through an opening in a two-dimensional rectangular channel is presented in Morse and Ingard [9, p. 487],

$$A = \rho\frac{\pi}{4}D^2\frac{8}{\pi^2}\ln\left(\frac{1}{2}\tan\left(\frac{\pi d}{4D}\right)+\frac{1}{2}\cot\left(\frac{\pi d}{4D}\right)\right). \tag{3}$$

Here d is the width of the opening and D the width of the channel, cf. left part of Fig. 3. The open-area ratio (perforation ratio) of the channel is

$$\tau = \frac{d}{D}. \tag{4}$$

Inserting the open-area ratio, and normalizing (3) by the added mass of a two-dimensional solid plate of width D, (2), one obtains a nondimensional expression for the added mass of flow through an opening in a channel,

$$\frac{A}{A_0} = \frac{8}{\pi^2}\ln\left(\frac{1}{2}\tan\left(\frac{\pi\tau}{4}\right)+\frac{1}{2}\cot\left(\frac{\pi\tau}{4}\right)\right). \tag{5}$$

The expression for one opening may be extended to the case of a channel with n_h equal openings, cf. right part of Fig. 3, that together yield an open-area ratio τ,

$$\frac{A}{A_0} = \frac{8}{n_h\pi^2}\ln\left(\frac{1}{2}\tan\left(\frac{\pi\tau}{4}\right)+\frac{1}{2}\cot\left(\frac{\pi\tau}{4}\right)\right). \tag{6}$$

As pointed out by Molin [6], the added mass goes to zero as the number of openings goes to infinity, regardless of the perforation ratio. For a perforated plate with perforation ratio τ consisting of n_h openings, (6) can be used to estimate the added mass coefficient for the low-KC limit for perforated plates close to sidewalls, that is, in channels. Sketches of the two cases with corresponding nomenclature as in (5) and (6) are presented in Fig. 3.

As part of verification of the present numerical viscous flow solver (to be presented in Section 4), two test cases have been simulated and compared to the analytical added mass expressions of (5) and (6).

3.2. Source method

A two-dimensional source panel method is presently implemented to calculate added mass coefficients for the low-KC limit. Unlike the analytical expression in (6), the source panel method can be used to calculate added mass coefficients for arbitrary configurations, in particular plates in both infinite fluid and channels.

The basis of the two-dimensional source panel method is the source-dipole formulation arising from Green's 2nd identity, where matching of the inner and outer potentials yields a method that depends on the source strengths only [10]. Hence, by distributing sources on the boundaries, the velocity potential can be determined everywhere in the fluid domain. In the present study, sources with constant strengths are distributed along discretized bodies and boundaries. The hydrodynamic heave added mass coefficients are then calculated by numerically integrating the contribution from the linearized pressure on the bodies in the vertical direction. Results from the source method is denoted BEM (boundary element method) in the present text. Numerical convergence is investigated. The code has been verified against analytical solutions for the added mass of simpler structures.

4. Numerical viscous flow solver

In addition to the source method described in Section 3.2, numerical results are obtained from solving the governing equations of incompressible and isothermal flows of a homogeneous Newtonian fluid with negligible bulk viscosity, the continuity and momentum (Navier–Stokes) equations,

$$\frac{\partial u_i}{\partial x_i} = 0, \tag{7}$$

$$\frac{\partial u_i}{\partial t} + u_j \frac{\partial u_i}{\partial x_j} = -\frac{1}{\rho}\frac{\partial p}{\partial x_i} + \nu \frac{\partial^2 u_i}{\partial x_j^2}. \tag{8}$$

Here u_i represents the velocity component in the x_i direction, ρ is the fluid density, p the pressure and ν the kinematic viscosity. Standard index notation is used. The solver is two-dimensional. Results from this solver are denoted CFD (computational fluid dynamics) in the present text.

The governing equations are solved with a fractional-step method, as that by Chorin [11], where the momentum equation is split into two steps,

$$\frac{u_i^* - u_i^n}{\Delta t} = -u_j \frac{\partial u_i}{\partial x_j} + \nu \frac{\partial^2 u_i}{\partial x_j^2}, \tag{9}$$

$$\frac{u_i^{n+1} - u_i^*}{\Delta t} = -\frac{1}{\rho}\frac{\partial p}{\partial x_i}. \tag{10}$$

Here n represents the present time-step, $n+1$ the next time-step, and $*$ an auxiliary step. Since the velocity field at $n+1$ is divergence free, (7), the divergence of (10) yields a Poisson equation for the pressure

$$\frac{\partial^2 p}{\partial x_i^2} = \frac{\rho}{\Delta t}\frac{\partial u_i^*}{\partial x_i}. \tag{11}$$

For each time step, the following solution procedure is performed:

1. Find the tentative velocity field from (9).
2. Use the tentative velocity field to calculate the pressure from (11).
3. Use the tentative velocity field and the calculated pressure to calculate the velocity from (10).
4. Extrapolate the lagged pressure to obtain second order temporal accuracy [12].

4.1. Discretization

The governing equations are solved on a Cartesian grid. The implementation allows for variable grid cell sizes. A staggered grid approach is chosen. A Crank–Nicolson based scheme for the time-stepping procedure of (9) is applied. The Crank–Nicolson method is based on central differencing and yields second-order temporal accuracy [13], without need for corrector steps. However, a drawback of the method is the time penalty of solving the intermediate velocity field in an implicit manner. The Crank–Nicolson method will yield higher accuracy than the fully implicit scheme. However, unphysical results can occur, and there are limitations to the time-step size in order to achieve physically plausible solutions [14].

The diffusion terms of (9), the pressure gradient terms of (10), as well as the terms of (11) are solved with central difference schemes. The discretization of these terms are made second-order accurate, taking into account variable cell sizes.

The non-linear advection terms of Eq. (9) are solved by using the known velocity field at the previous time-step. Consequently, the present approach is not fully second-order accurate in time with regards to the advection terms, despite being based on a Crank–Nicolson approach. Upwind schemes are used to discretize the advection terms. First, second, and third order upwind schemes are tested. The first order scheme approximates the differential based on values of the present cell and the upstream cell, whereas the second order scheme includes information about the present cell and two upstream cells. The third order scheme also includes information about one cell downstream. Different combinations of the first, second and third order schemes have been applied as follows

$$\frac{\partial u_i^k}{\partial x_j} = (1-\sigma-\epsilon)\left.\frac{\partial u_i^k}{\partial x_j}\right|_{1st} + \sigma\left.\frac{\partial u_i^k}{\partial x_j}\right|_{2nd} + \epsilon\left.\frac{\partial u_i^k}{\partial x_j}\right|_{3rd}. \tag{12}$$

Here σ and ϵ are constants, $0 \leq \sigma + \epsilon \leq 1$, and k is either n or $*$. Increasing σ and/or ϵ increases the order of the discretization, potentially increasing the accuracy of the calculation. Simulations are performed with (σ, ϵ) set to $(0, 0)$, $(0.5, 0)$ or $(0, 0.5)$ yielding pure first order schemes, or hybrid schemes based on combinations of first order with either second or third order schemes. Only small differences are found in the resulting hydrodynamic coefficients between the different upwind scheme approaches, typically within 5 %. However, using schemes based on higher order approaches are found to give stability issues in some cases, consistent with numerical theory, while such problems are not encountered with the first order scheme. Additionally, the higher-order schemes will increase the computational cost since a larger matrix system must be solved. For consistency, all presented CFD results are those obtained using the pure first order scheme, that is, $(\sigma = 0, \epsilon = 0)$.

As for the central difference schemes, the upwind schemes are constructed by taking into account the potentially varying cell sizes. Additionally, since a staggered grid is used, the velocity components used to calculate cross-derivative advection terms, are interpolated based on the four surrounding velocity components, in order to determine the direction of the flow. As for the differentials, this interpolation accounts for the possibility of variable cell sizes.

4.2. Boundary conditions

On the boundaries of the fluid domain, the prescribed harmonically oscillating fluid velocity is set,

$$u = 0, \tag{13a}$$

$$w = W \sin(\omega t), \tag{13b}$$

where u is the fluid velocity in the x-direction and w that in the z-direction (coordinate system, cf. Fig 1). No-slip conditions are enforced on the models,

$$u = 0, \tag{14a}$$

$$w = 0. \tag{14b}$$

The pressure gradient is set to zero on all boundaries of the CFD domain,

$$\frac{\partial p}{\partial n} = 0. \tag{15}$$

Sensitivity tests were performed to avoid domain boundary influence, by placing the boundaries with different distances from the body. Typically, the domains are of sizes $\frac{l}{D} \approx 15$, with l being the domain length and width.

4.3. Simulation parameters

Three parameters are constant in all simulations, the period of oscillation, $T = 1.0\,\mathrm{s}$, the density, $\rho = 1000\,\mathrm{kgm^{-3}}$, and the kinematic viscosity, $\nu = 1.0 \times 10^{-6}\,\mathrm{m^2s^{-1}}$. This will ensure similar Reynolds number in the simulations as in the present experimental investigation.

The time steps in the simulations are set to

$$\Delta t = \min\left(0.005T,\ 0.4\frac{\min\left(\Delta x, \Delta z\right)}{W}\right), \tag{16}$$

where min $(\Delta x, \Delta z)$ is the length of the smallest cell size. The first condition ensures a minimum of 200 time-steps per period of oscillation, while the latter was chosen based on sensitivity studies on the time-step size (not presented).

Limiting the number of oscillation periods reduces the number of time-steps needed, and thereby the computational cost of the simulation. A sensitivity study (not presented) on the number of oscillation periods needed to obtain oscillation period independent results, was performed. Based on our findings, the added mass and damping coefficients are calculated based on oscillation period 4, 5 and 6. The three first oscillations, 1-3, are ignored due to start-up of flow.

4.4. Grid cell size sensitivity

A grid sensitivity study has been carried out for a plate with 80 mm total hole width and 352 mm total solid width, that is, the plate is 432 mm wide and has a perforation ratio of $\tau = 0.185$. The plate thickness is set to $t = 8\,\mathrm{mm}$. The number of plate elements is 11, with 10 holes in between. These parameters are chosen such that three grids can be tested, keeping all other parameters the same, i.e. using two, four, and eight fluid cells between each plate element, and, respectively, eight, 16, and 32 solid cells to model the plate elements, as well as having two, four, and eight cells across the thickness of the plate. This fictitious plate resembles the plates that have been tested experimentally in the present study. The time-step size used in this sensitivity analysis was set based on the finest grid, cf. (16).

In order to have a fine resolution around the bodies, but limit the computational time, stretched grids are used in the simulations. We define a fixed cell size, $\Delta = \Delta x = \Delta z$ in the vicinity of the plate, and geometrically

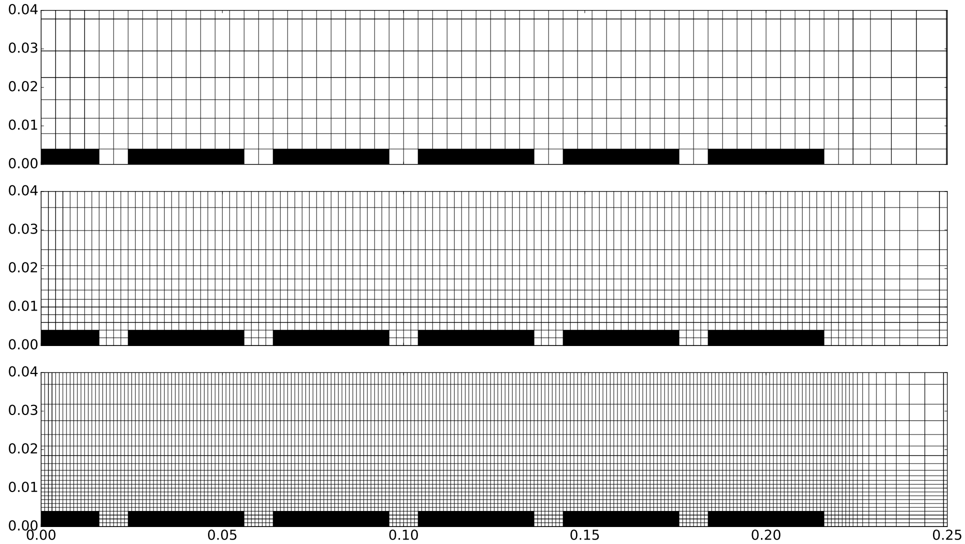

Figure 4: Upper right parts of the fine region of the grids tested in the grid cell size sensitivity. $\Delta = 4\,\mathrm{mm}$ (top), $2\,\mathrm{mm}$ (middle), and $1\,\mathrm{mm}$ (bottom). Total plate size: $D = 432\,\mathrm{mm}$, $t = 8\,\mathrm{mm}$. Total domain size is $6\,\mathrm{m} \times 6\,\mathrm{m}$.

increase cell sizes towards the boundaries of the domain. Based on sensitivity tests on stretching (not presented), the increase in adjacent cell size in the stretched regions is set to 20 %. The stretching will increase the cell sizes up to a given maximum value, typically set to 50 mm, beyond which a constant cell size is applied. Such relatively large cell sizes are justified by that the spatial variation of the flow is small far away from the body. The total number of grid cells are 34 672 ($\Delta = 4\,\mathrm{mm}$), 56 176 ($\Delta = 2\,\mathrm{mm}$), and 101 376 ($\Delta = 1\,\mathrm{mm}$), for the three grids in the grid cell size sensitivity test. A section of the fine regions of these grids is shown in Fig. 4. The grids are symmetric with respect to both axes. To increase readability, such that the smallest grid cells can be seen, only the upper right parts ($x \geq 0$, $z \geq 0$) of

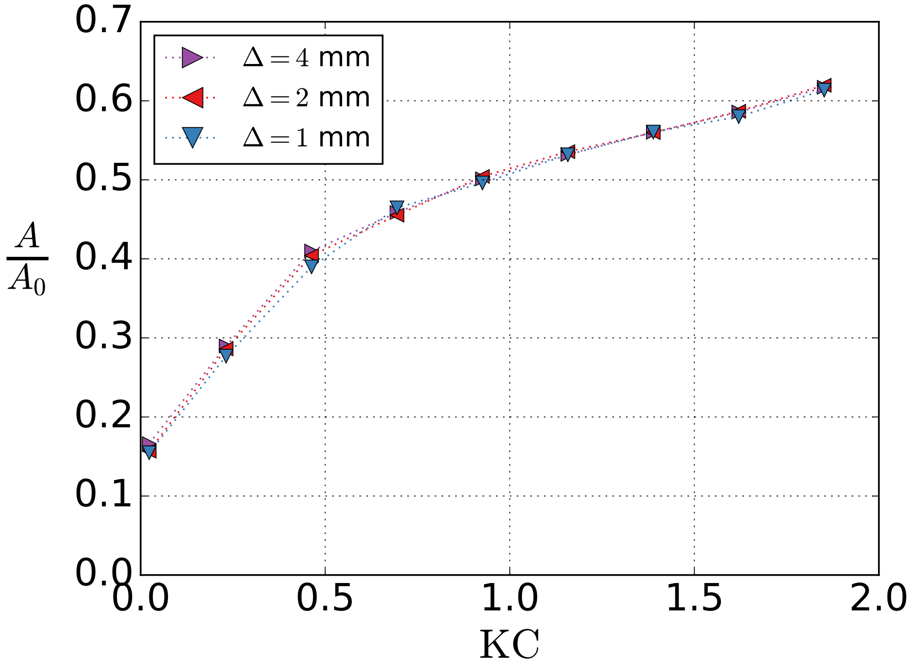

Figure 5: Added mass coefficients predicted by the present CFD for perforated plates of $\tau = 0.185$, modeled with different grid cell sizes, $\Delta = 4\,\text{mm}$, $2\,\text{mm}$, and $1\,\text{mm}$, in the fine region close to the plate. The number of plate elements is fixed to 11.

the fine regions of the grids (and perforated plate) are shown.

The results from the grid size sensitivity are presented in Figs. 5 and 6. Except for minor differences in the damping coefficients, the results are nearly insensitive to the grid size within the tested range of Δx, Δz. Note in particular that using two fluid cells between each plate element is sufficient when discretizing perforated plates with the present numerical viscous flow solver. It may be somewhat surprising that so few cells over the gap is sufficient. Later in the text, we demonstrate good agreement with the

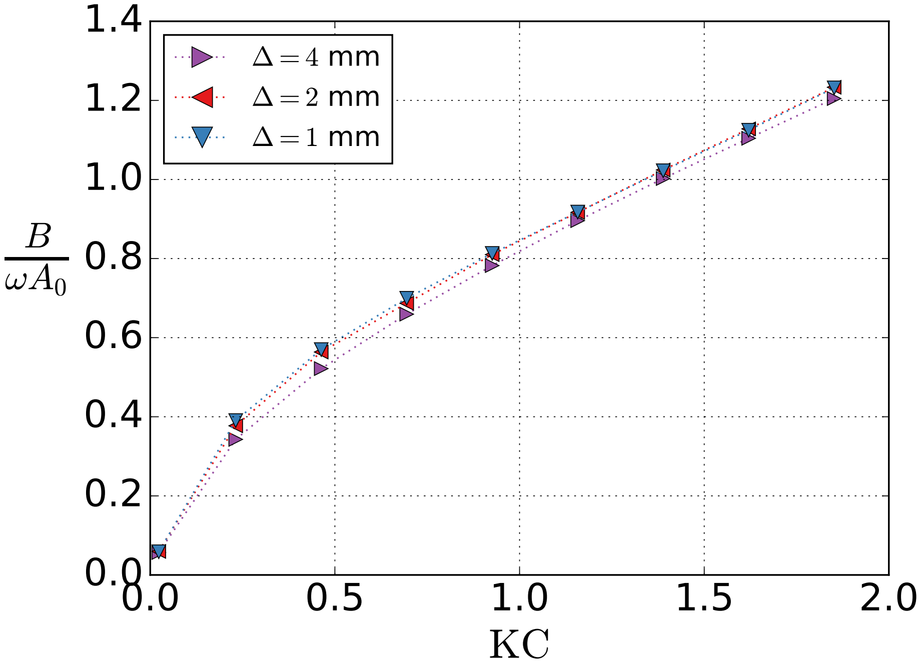

Figure 6: Damping coefficients predicted by the present CFD for perforated plates of $\tau = 0.185$, modeled with different grid cell sizes, $\Delta = 4\,\text{mm}$, $2\,\text{mm}$, and $1\,\text{mm}$, in the fine region close to the plate. The number of plate elements is fixed to 11.

experiments, using similar grids.

Testing the grid cell size sensitivity is not trivial, in general, and also when modeling a perforated plate with a numerical viscous solver. This is related to restrictions that follows when modeling such a structure with the constraints of a Cartesian mesh. The perforation ratio of the plate must be the same for all grids, hence there are constraints on both the plate elements with solid cells, and the fluid cells between them. Further, in order to have flow through the openings of the plate, there must be at least two fluid cells

Table 2: Relevant parameters in the numerical hole size sensitivity study, carried out with the present CFD. n and n_h refers to number of plate elements and holes, respectively. l_h refers to hole size.

n	$n_h \times l_h$
2	1× 78 mm
4	2× 25.5 mm and 1× 27 mm
7	2× 12 mm and 4× 13.5 mm
14	13× 6 mm
27	26× 3 mm

between each plate element due to the use of a staggered grid system. At the same time, these openings are small, such that increasing the number of fluid elements between each plate element will increase the computational time considerably. Even if larger hole sizes are used, there is still the problem of modeling the thickness of the plate correctly.

4.5. Hole size sensitivity

Different numerical hole sizes have been tested. The total number of solid cells, 228, and fluid cells, 52, along the width of the plate are kept constant, such that the perforation ratio in all tests are $\tau = \frac{52}{280} = 0.19$. Further, the same grid and setup are used, such that only the plate elements have been changed when performing the different simulations. Five different hole size setups, presented in Table 2, are tested.

The results from the sensitivity study on the numerical hole size are presented in Figs. 7 and 8. As expected, clearly, the number of plate elements,

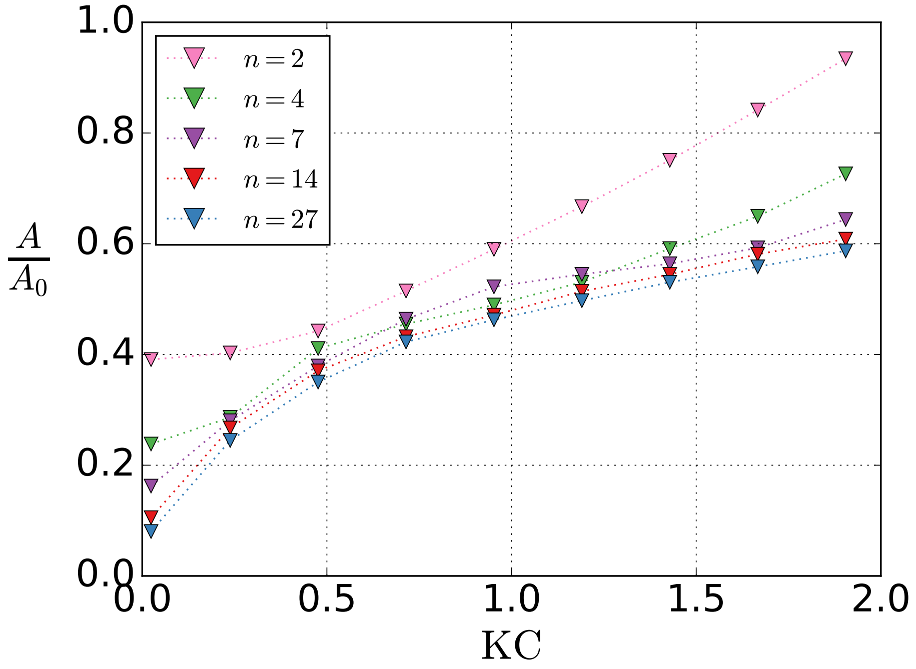

Figure 7: Added mass coefficients predicted with the present CFD for perforated plate models with $\tau = 0.19$. Comparison of predictions with different number of plate elements, 2, 4, 7, 14, and 27, cf. Table 2.

and corresponding hole size, is an important factor at low KC for the added mass coefficient. However, and most important, there is in general little difference between the four smallest hole sizes simulated, for $n \geq 4$. This applies in particular for damping. For added mass, $n \geq 7$ may be a better limit.

A possible explanation is the importance of flow separation at the plate-ends, which may dominate the damping contribution no matter the hole size. Consistent with the present results, two previous experimental studies

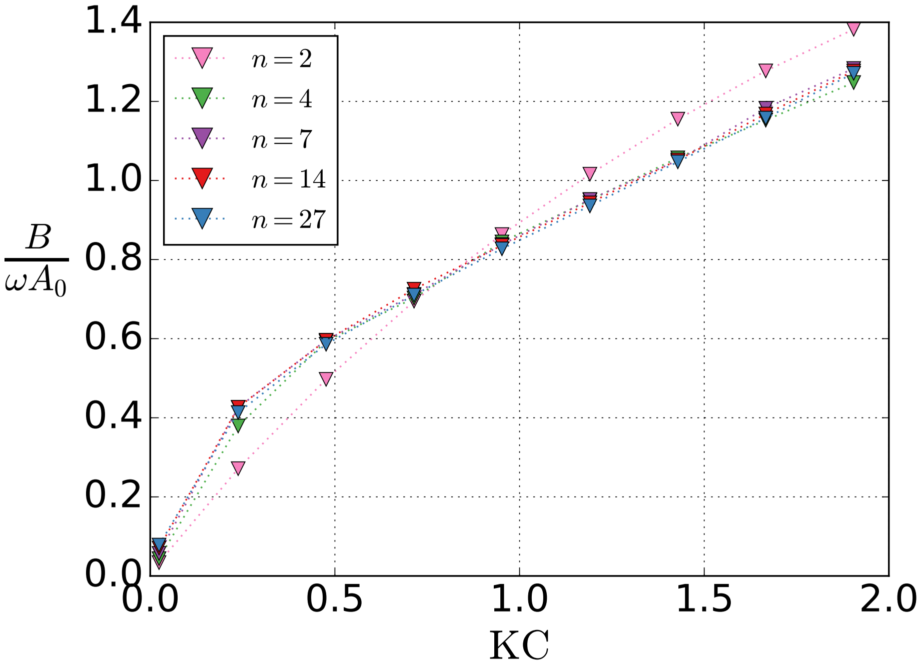

Figure 8: Damping coefficients predicted with the present CFD for perforated plate models with $\tau = 0.19$. Comparison of predictions with different number of plate elements, 2, 4, 7, 14, and 27, cf. Table 2.

have reported similar negligible hole size sensitivity [5, 8]. However, both these studies are limited to relatively low perforation ratios ($\tau = 0.05$ [5] and $\tau = 0.1$ [8]) with a limited number of hole sizes and low KC numbers. If the present numerical results for the plate with only one hole ($n = 2$) is disregarded, the differences are small. Consequently, it seems that the number of plate elements should not be of major importance for relevant KC numbers, as long as there are at least three holes on the plate. However, there may be numerical benefits of using more holes; using more holes seems

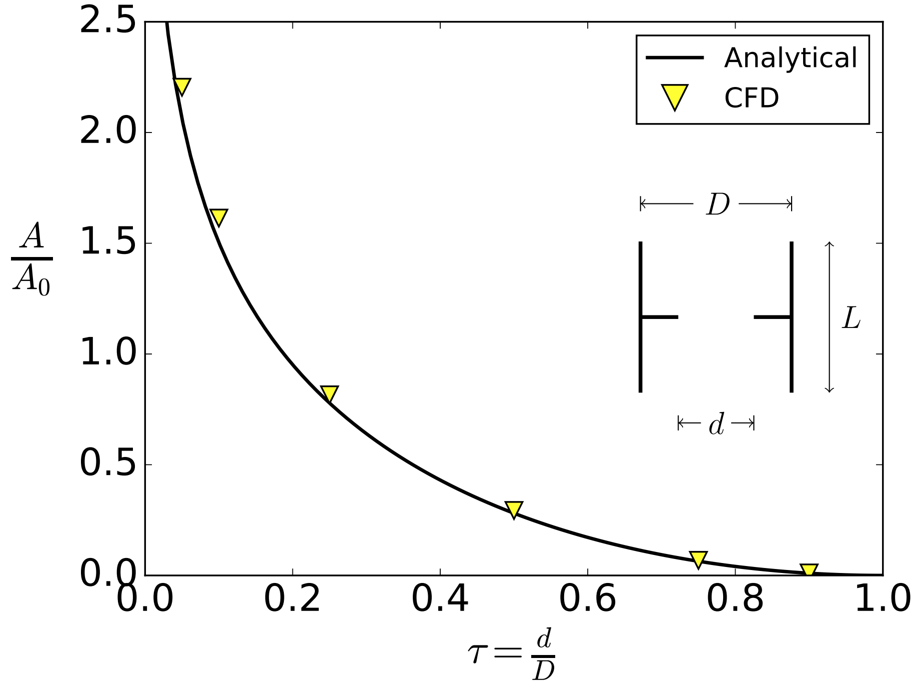

Figure 9: Added mass coefficient as function of the perforation ratio, $\tau = \frac{d}{D}$, due to oscillating flow through a slit in a 2D channel. "CFD" refers to predictions by the present CFD, run with small $\mathrm{KC} = \frac{WT}{D} = 0.01$. "Analytical" refers to Eq. (5).

favorable in terms of domain size needs and numerical stability, due to less stagnation (potential flow effects) of the flow and thereby less need for a large domain.

4.6. Simple channel flow validation cases

Oscillating flow through an opening in a channel is simulated with the presently developed CFD code at low KC-number; $\mathrm{KC} = 0.01$, with D being the channel width. The opening is discretized by using 320 grid cells across

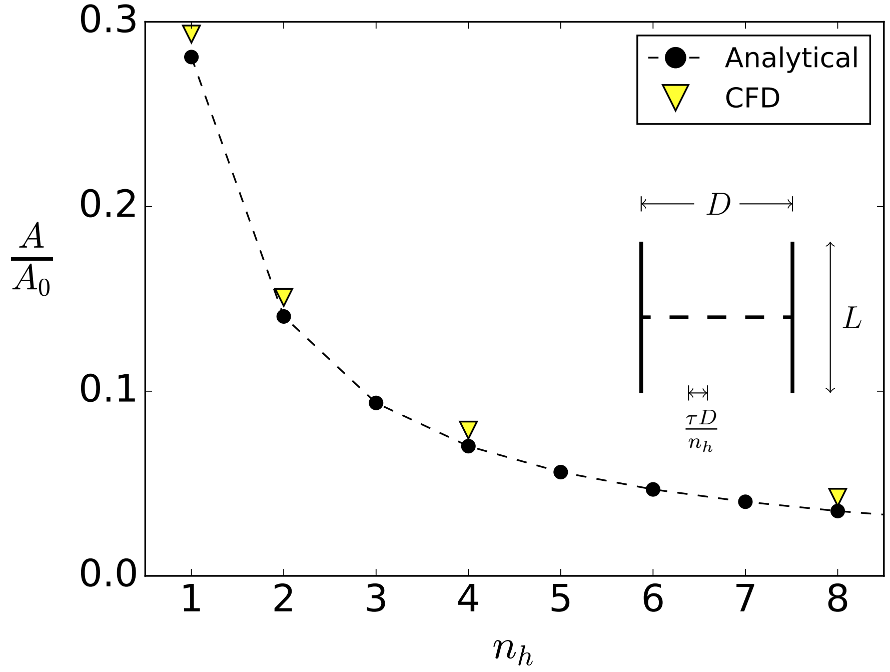

Figure 10: Added mass coefficient as function of the number of openings, n_h, due to oscillating flow through a series of openings in a 2D channel. “CFD” refers to predictions by the present CFD, run with small KC $= \frac{WT}{D} = 0.01$. “Analytical” refers to Eq. (6).

the channel width and one grid cell across the opening height. The channel length is $\frac{l}{D} = 5$, and the total number of grid cells is 32 480. The numerical results are compared with the analytical expression (5), and the comparison is presented in Fig. 9. The curve and trend predicted with the analytical expression is well captured by the numerical simulations.

Next, the effect of number of openings is investigated. For the case of $\tau = 0.5$, four number of openings ($n_h = 1$, 2, 4 and 8) were simulated, and compared with the analytical expression (6). The resulting added mass

Table 3: Relevant parameters in the numerical discretizations of the P19 and P28 plates, as used in the present CFD computations. The plates are discretized using $n = 27$ plate elements. Total width and thickness of the plates are, respectively, $D = 420\,\mathrm{mm}$ and $t = 3\,\mathrm{mm}$. The number of (#) solid and fluid grid cells along the width and thickness of the plates are indicated.

	P19	P28
Fine region cell size, Δ	1.5 mm	1.5 mm
Hole size, l_h	3.0 mm	4.5 mm
# plate width solid cells	228	202
# plate width fluid cells	52	78
# plate thickness cells	2	2

coefficients are presented in Fig. 10. Again, the trend predicted by the analytical expression is captured by the numerical results.

This concludes the sensitivity tests and verification studies for KC → 0 of our CFD code. In the remaining parts of the paper, the main results of perforated plates of 19 % and 28 % perforation ratios are presented at a large range of KC numbers.

5. Results

5.1. Perforated plates in oscillating open flow

The main results from the present study are given in this section. Numerical and experimental results for the hydrodynamic force coefficients in oscillating open flow conditions of the two perforated plates (P19 and P28)

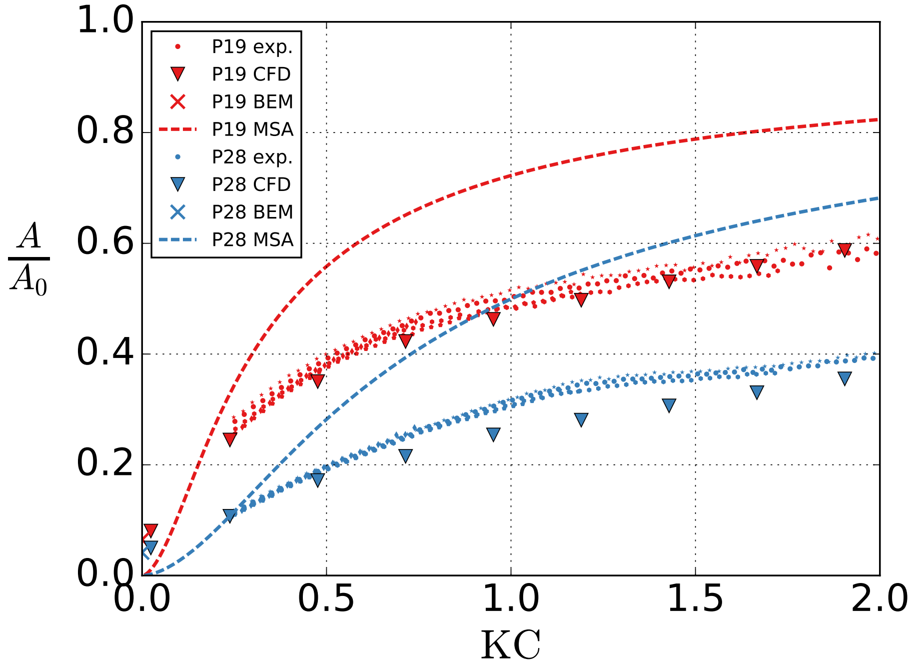

Figure 11: Added mass coefficients from present CFD simulations (one period, $T = 1.0\,\mathrm{s}$), the present experiments (five different periods), source panel results (crosses at KC = 0), and Molin's semi-analytical (MSA) method using a discharge coefficient $\mu = 0.5$ [6]. Recommendations by DNV GL for use in the low-KC limit [15, Section 3.3.4] and for all KC numbers [15, Section 4.6.4] yield, respectively, $\frac{A}{A_0} = 0.51$ and $\frac{A}{A_0} = 0.78$ ($\tau = 0.19$), and $\frac{A}{A_0} = 0.37$ and $\frac{A}{A_0} = 0.54$ ($\tau = 0.28$).

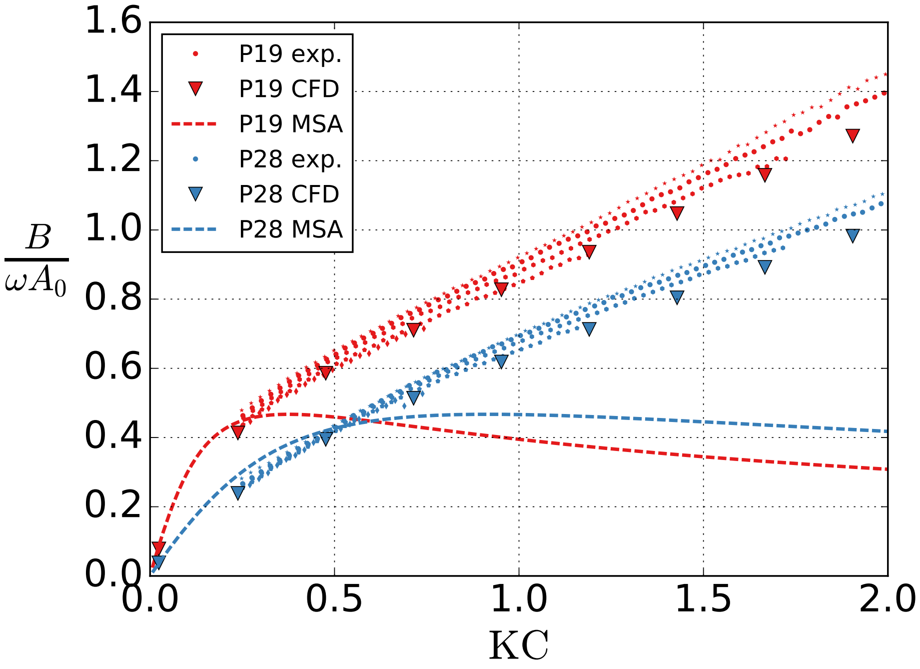

Figure 12: Damping coefficients from present CFD simulations (one period, $T = 1.0\,\mathrm{s}$), the present experiments (five different periods), and Molin's semi-analytical (MSA) method using a discharge coefficient $\mu = 0.5$ [6].

are provided. The term *open* is here used to emphasize that the outer boundaries are far from the plate, as opposed to the channel flow results presented in Section 5.2. The configuration is nearly that of infinite fluid, except that there is a free surface and a tank floor, cf. Fig. 1. Free-surface effects are investigated and found to be small.

In the experiments, the perforated plates are placed in the middle of the water tank, approximately 6.5 m from each side wall, and 0.5 m from the tank bottom and free surface. This corresponds to a ratio between the distance

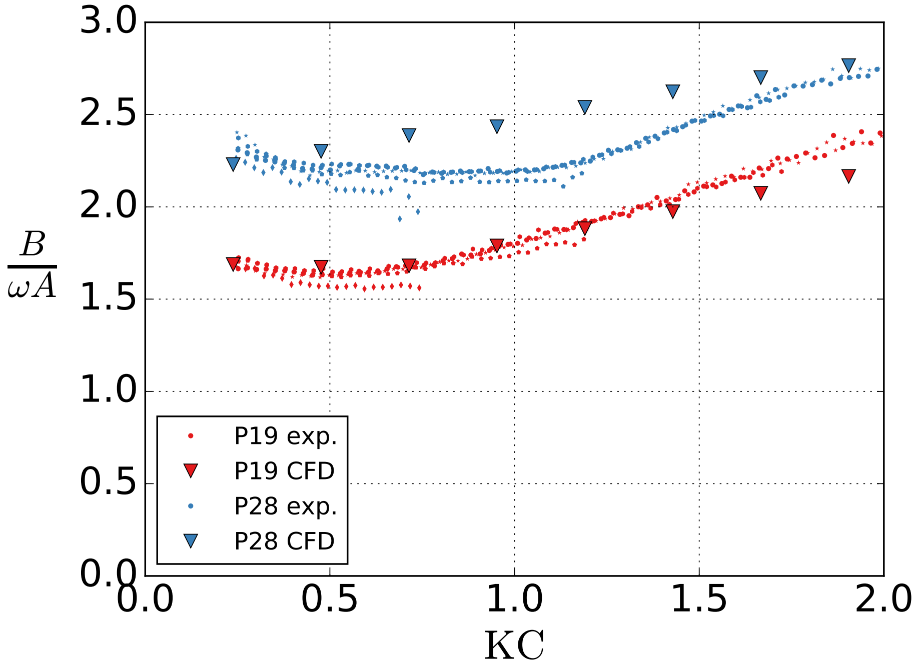

Figure 13: Ratio between damping force and added mass force, cf. Figs. 11 and 12.

to the free surface compared to the amplitude of motion of approximately 30 for the smallest amplitudes tested, but only four for the largest amplitudes tested. The numerical simulations are performed with the plates 3 m from all four computational boundaries, hence the domain size to plate width ratio is $\frac{l}{D} = \frac{6}{0.42} = 14.3$. There is no free surface in the CFD simulations. A large simulation domain is necessary in order to avoid numerical instabilities and unphysical results, since the velocity is forced to prescribed values at the boundaries. Hence, the present CFD simulations provide infinite fluid results, whereas the experimental investigations are in principle affected by free-surface effects. However, in [1], we concluded that these were negligible based on small measured radiated waves.

The final discretization in CFD was chosen based on the grid sensitivity study presented in Section 4.4. Details on the discretization are given in Table 3. In addition to the experimental and numerical viscous flow results, added mass results for KC $\to 0$ are predicted by the present BEM with identical plates as that in the CFD.

We have included hydrodynamic coefficients obtained using Molin's semi-analytical method [6] with a discharge coefficient $\mu = 0.5$, abbreviated MSA in the plot legends. The value for the discharge coefficient was chosen based on Blevins [16, pp. 314–315] and Molin [6]. Included are also added mass estimates from the recommended practice by DNV GL for modeling and analysis of marine operations [15].

The added mass coefficients are presented in Fig. 11. The small markers represent experimental results (five different periods), whereas the larger triangles represent the CFD results. Source panel results are indicated by crosses at KC $= 0$. There is, in general, good agreement between the experimental and CFD results for both perforation ratios. P19 yields the best comparison, while some of the numerical results for P28 underpredict. Nevertheless, these differences are relatively small.

The damping coefficients for the two perforated plates are presented in Fig. 12. The results from the numerical simulations agree well with the experimental values.

For a given KC number, both the added mass coefficient and damping coefficient decrease with increasing perforation ratio. The added mass co-

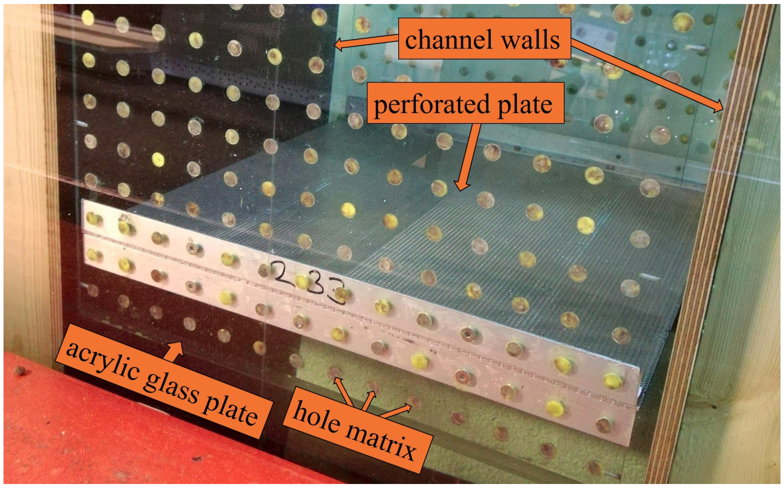

Figure 14: A photo illustrating the present experimental setup of the tests of oscillating plates in a channel. In particular, the channel walls are indicated.

efficient decreases the most, such that the hydrodynamic force balance, $\frac{B}{\omega A}$, increases with increasing perforation ratio. The ratio $\frac{B}{\omega A}$ is presented in Fig. 13. The hydrodynamic load on both plates are found to be dominated by damping for the whole range of KC numbers. In particular, for P28, the damping force is clearly dominant over the added mass force. This has practical importance, but has not been reported in previous studies, prior to [1]; previous studies have focused on the amplitude dependent added mass.

5.2. Perforated plates in oscillating channel flow

As an attempt to investigate the forces on the plates without allowing the massive flow separation at the plate-ends, experiments and numerical simulations were set up in which the plates were placed inside two walls yielding a setup that mimics oscillating channel flow conditions. These walls were placed approximately 2 cm from the ends of the perforated plates in both

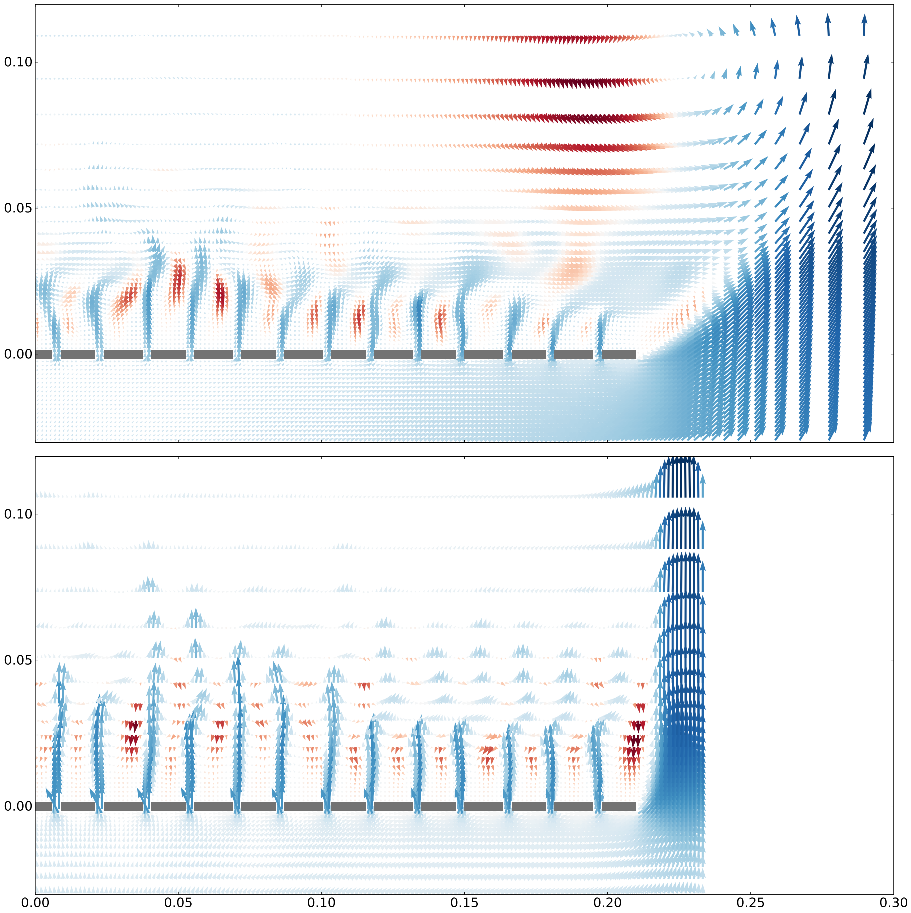

Figure 15: Flow visualization from numerical simulations. The subplots show the right part of the perforated plate with $\tau = 0.19$ in open (top) and channel (bottom) conditions. The velocity amplitude is $W = 0.4\,\mathrm{ms}^{-1}$, corresponding to $\mathrm{KC} = 0.94$. The flow visualizations are captured at a time-instant 30 % into an oscillation period. Blue arrows are used for positive vertical velocity, red for negative.

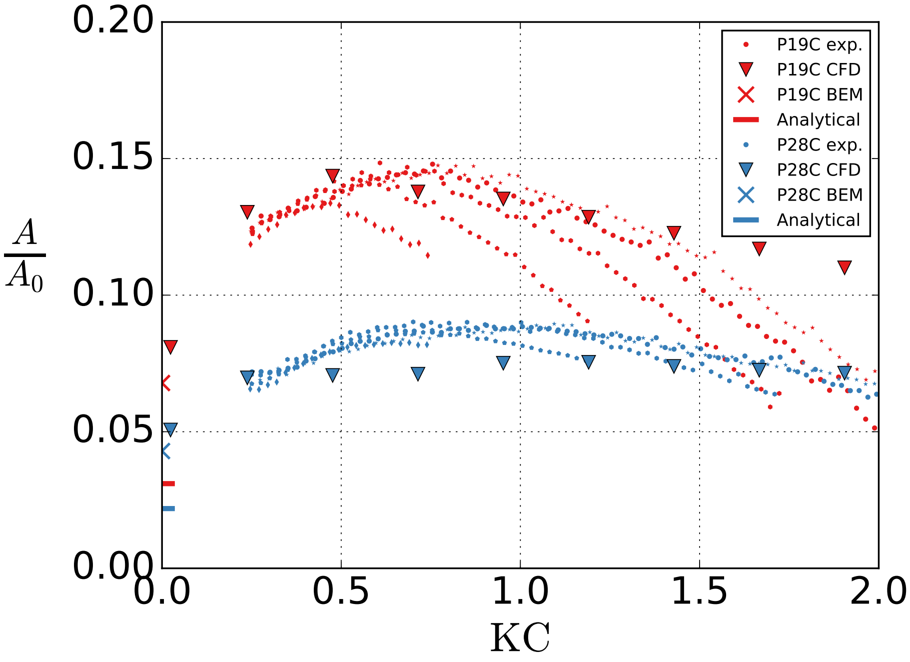

Figure 16: Added mass coefficients for perforated plates in channel flow conditions. Present CFD (one period, $T = 1.0\,\mathrm{s}$) compared with present experimental results (five different periods), present source panel results (BEM), and the analytical expression of Eq. (6). C refers to channel.

the experiments and the numerical simulations. Results from the channel flow investigations are denoted with a C, that is, P19C and P28C for, respectively, the perforated plates with 19 % and 28 % perforation ratios. A photo of the experimental setup is presented in Fig. 14.

When the plates are forced to oscillate inside the channel, vortex shedding from flow separation at the plate-ends will be limited, but so will the possibility for the fluid to flow around the plate, since the water is forced to

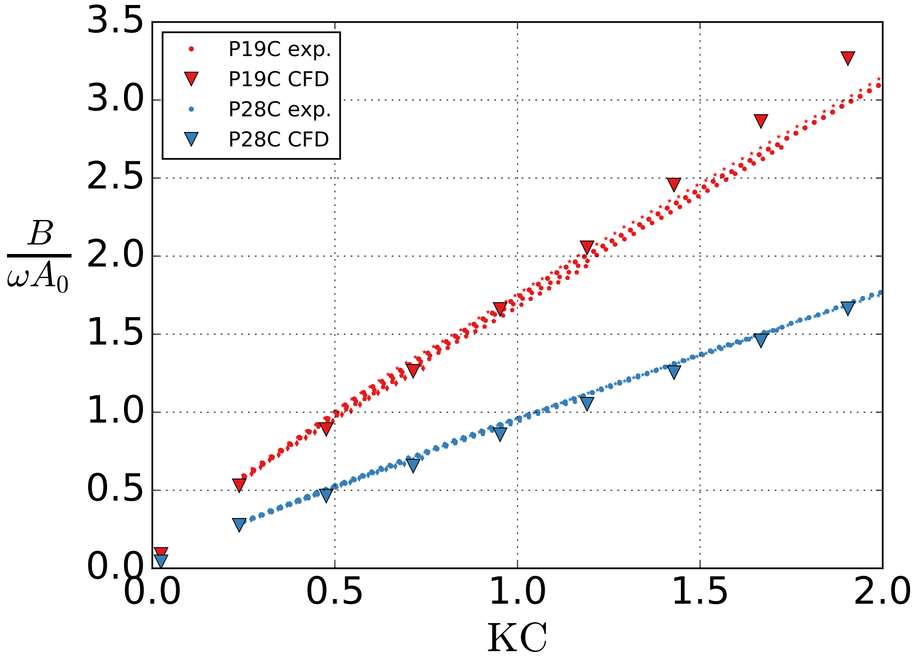

Figure 17: Damping coefficients for perforated plates in channel flow conditions. Present CFD (one period, $T = 1.0\,\mathrm{s}$) compared with present experimental results (five different periods). C refers to channel.

pass the plate either through the perforated openings or through the gaps between the plate-end and the channel walls, due to continuity of mass. As a result, the force that acts on the plate will be in almost exact phase with the velocity of the ambient flow or plate, and therefore completely dominated by a large damping force (and correspondingly large damping coefficient), and only yield a minor added mass coefficient.

Differences between open and channel flow conditions are illustrated in Fig. 15. Here, flow visualizations, in terms of velocity vector plots, from the

Table 4: Linear regression analysis of damping coefficients as function of KC number. The analysis is based on the experimental results (Exp.) and numerical simulations (CFD) of oscillating perforated plates in a channel, P19C and P28C. r^2 is the coefficient of determination.

Method	Intercept	Slope	r^2
P19C Exp.	0.27	1.43	0.999
P19C CFD	0.08	1.67	1.000
P28C Exp.	0.11	0.83	0.999
P28C CFD	0.05	0.85	0.999

Table 5: Linear regression analysis of the ratio between hydrodynamic force amplitude as function of KC in channel flow and open conditions. The analysis is based on the experimental results (Exp.) and numerical simulations (CFD) of the perforated plate models. r^2 is the coefficient of determination.

Method	Intercept	Slope	r^2
$\tau = 0.19$ Exp.	0.97	0.63	0.947
$\tau = 0.19$ CFD	0.99	0.84	0.988
$\tau = 0.28$ Exp.	0.91	0.29	0.957
$\tau = 0.28$ CFD	0.98	0.36	0.960

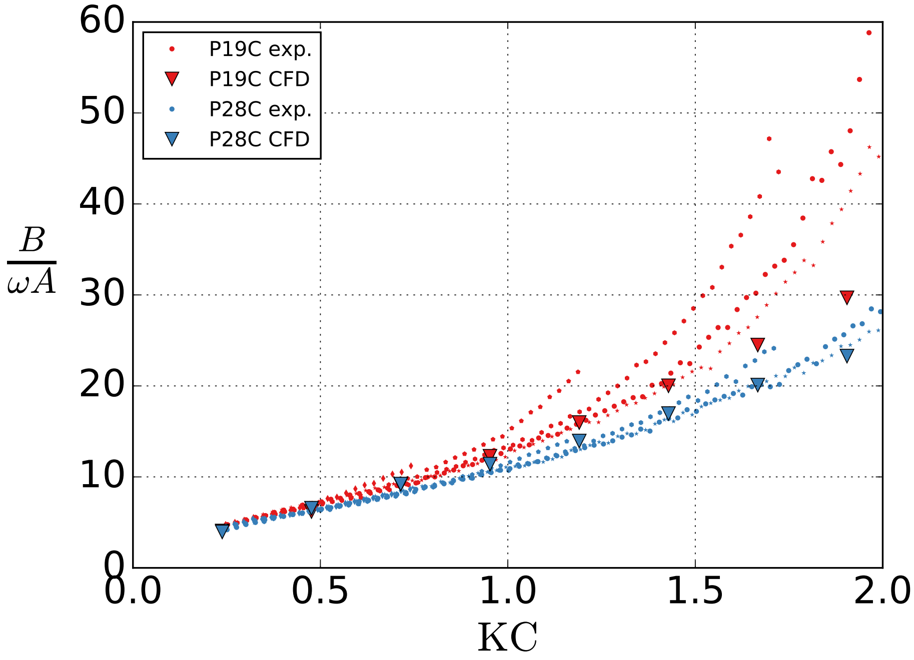

Figure 18: Ratio between damping force and added mass force, cf. Figs. 16 and 17.

numerical simulations of the perforated plate with $\tau = 0.19$, are presented. The velocity amplitude is $W = 0.4\,\mathrm{ms}^{-1}$, corresponding to KC = 0.94. The plots are obtained at a time-step 30 % into an oscillation period, that is, the vertical velocity is $w = 0.4 \sin(0.6\pi)$ at the boundaries. In both open (top subplot) and channel (bottom subplot) conditions, the fluid flow is accelerated in the vertical direction through the perforations of the plates. Further, in open conditions, a large vortex is developed from the plate-end (centered in $x = 0.224$, $z = 0.094$ at this time instant). For channel flow conditions, a similar vortex is not seen. Instead, the fluid between the plate and the channel wall is accelerated in the vertical direction, similar to the acceleration of fluid through the openings.

The numerical and experimental channel flow added mass coefficients agree reasonable well, as seen in Fig. 16. For P19C, the experimental results show considerable period dependence, where the drop in added mass occurs at different KC numbers for different periods of oscillation. This can be related to free-surface effects, not captured in the CFD simulations.

The analytical expression (6) does not account for the thickness of the plate elements, and underpredicts the added mass coefficients in the low-KC limit. The number of plate elements are here 27, and their thickness is important, $\frac{t}{D_i} \approx 0.25$, with D_i being the width of each plate element. In tests with the BEM where the thickness is reduced to $\frac{t}{D_i} \approx 0.025$, the added mass coefficients reduce considerably (P19C: $-38\,\%$, P28C: $-32\,\%$), and are thus more in line with (6).

The damping coefficients from the oscillating channel flow investigation are presented in Fig. 17. Both the experimental and numerical results indicate a nearly perfect linear relation between the damping coefficient and KC, meaning that a quadratic pressure-loss model is very good for this setup. Resulting interceptions (damping at zero KC) and slopes from linear regression of the experimental and numerical results, are presented in Table 4. The coefficients of determination confirms the perfect linearity ($r^2 = 1$) with KC.

The total hydrodynamic force on the perforated plates is larger in channel flow conditions compared to open conditions. A linear regression analysis is presented in Table 5. The analysis is here performed between the increase in hydrodynamic force in channel flow compared to open conditions, as a function of the KC number. The increase in force is found to be approximately linear with the KC number ($r^2 \approx 1$). The intercept refers to the value at $\mathrm{KC} = 0$. The analysis shows that all intercepts are close to 1, meaning that at very small KC numbers, the total hydrodynamic force is approximately the same in channel as in open flow conditions. Further, the slope is dependent on the perforation ratio; the total hydrodynamic force on the plate with 19 % perforation ratio is found to increase more rapidly with increasing KC number, compared to the plate with 28 % perforation ratio.

Figure 18 is included to illustrate the damping dominance in channel flow conditions. Even at small KC numbers, the hydrodynamic force on the plates are completely dominated by damping. The fact that the hydrodynamic force on the plates increase considerably in channel flow conditions, and that the damping force is dominating completely, can have relevance for operations performed in an environment restricted by walls or boundaries. Moonpool operations, where objects are lowered through an opening in the hull of the ship, is a relevant example.

5.3. 3D effects and comparison with 3D experiments

A 2D simplification of the 3D experiments performed by An and Faltinsen [2] has been simulated with the present CFD. Their study included one plate with perforation ratio $\tau = 0.08$ and one plate with $\tau = 0.16$. The plates are numerically modeled as being 440 mm wide, to match the square root of the plate area (520 mm × 365 mm) in their experiments.

The resulting coefficients are presented in Figs. 19 and 20 with comparisons to digitization of their experimental results. The experimental results were made nondimensional by the 3D solid plate potential flow added mass,

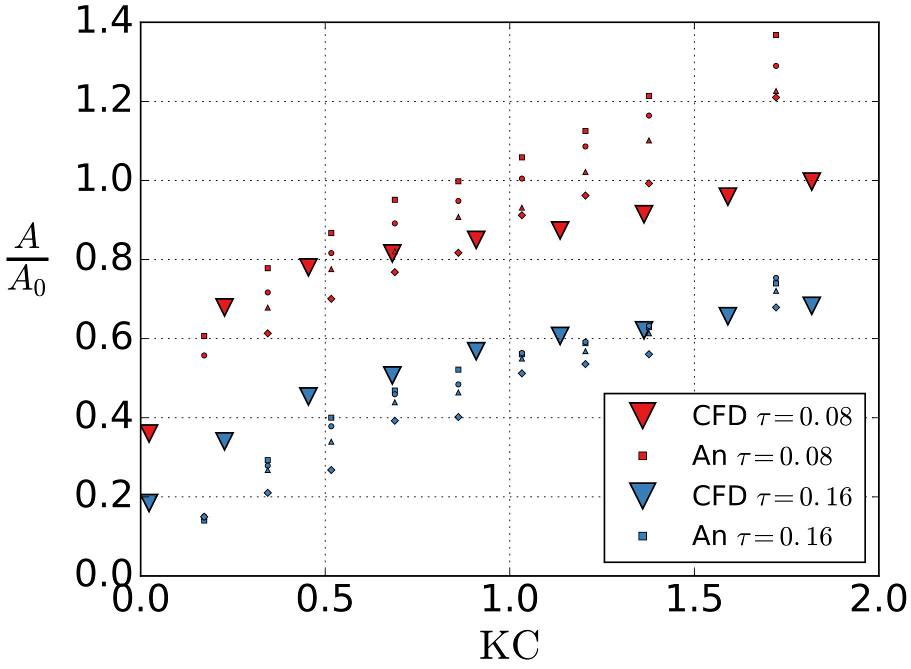

Figure 19: Added mass coefficients for 2D perforated plates as predicted by the present CFD, compared with experimental (four periods) 3D results by An and Faltinsen [2].

numerically calculated by An and Faltinsen [2]. Different markers are used to indicate four periods of oscillation in the experiments; $T = 1.5\,\mathrm{s}$ (squares), $T = 2.0\,\mathrm{s}$ (circles), $T = 2.5\,\mathrm{s}$ (triangles), and $T = 3.0\,\mathrm{s}$ (diamonds).

There is in general reasonable agreement between the present 2D numerical simulations and the 3D experiments. There is larger difference in the added mass of the two plates in the experimental investigation than what is found in the numerical simulations. This can be related to obvious differences between a 3D experiment and a 2D simulation. Further, free surface effects may be of importance. Since the densest perforated plate has a per-

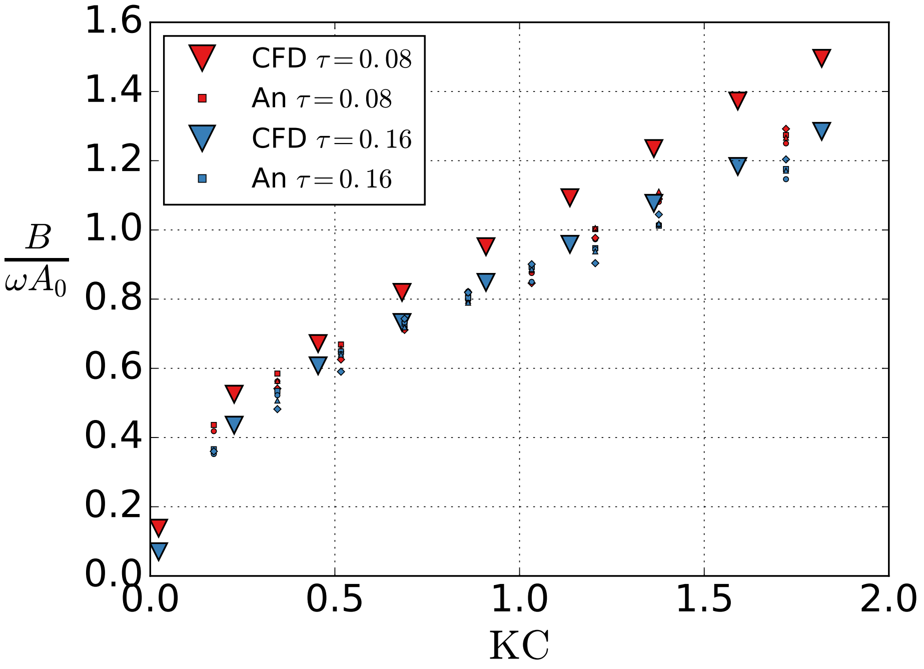

Figure 20: Damping coefficients for 2D perforated plates as predicted by the present CFD, compared with experimental (four periods) 3D results by An and Faltinsen [2].

foration ratio of only $\tau = 0.08$, it is likely to cause non-negligible free surface deflections at the largest amplitudes of motions. This plate is more sensitive to the period of oscillation than the less dense plate, an indication that the presence of the free surface may be of importance for the force on the plate.

As elaborated earlier, plate-end flow separation is important for the hydrodynamic force on perforated plates, in particular for the damping. The flow separation will occur on two sides of a two-dimensional plate, and on four sides of a three-dimensional plate. Nevertheless, the damping coefficients agree reasonable well when comparing the 2D simulations and the 3D

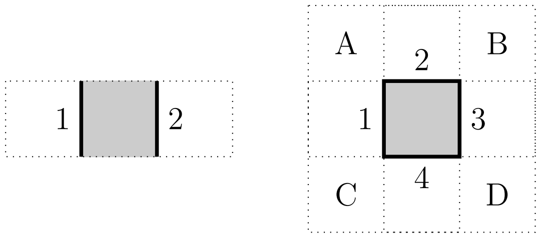

Figure 21: Explanation of parameters used in discussion of 2D (left) vs 3D (right) plate flow. The flow will separate at the plate-ends in both cases (numbered edges), but is allowed to circumvent the plate without separation in 3D (A, B, C and D).

experiments. We identify two effects in this respect. 1) Interaction between the flow separation from the four sides in 3D is more dominant than the interaction from flow separation at the two sides in 2D. 2) The flow has more freedom to circumvent the plate in 3D. This is illustrated in the sketch in Fig. 21. The flow will separate on the sides 1 and 2 in the two-dimensional case, and from sides 1, 2, 3 and 4, including their corners, in the three-dimensional case. However, the freedom to flow in the intermediate quadrants A, B, C and D without separation is only possible in 3D.

6. Conclusion

A two-dimensional numerical viscous flow solver based on the Navier–Stokes equations has been developed in order to investigate hydrodynamic forces on perforated plates in oscillating flow conditions, which has relevance in several marine applications, for instance in relation to marine operations with complex subsea modules. In order to validate and verify the solver, experimental, analytical and numerical methods have been compared, and sensitivity studies have been performed. Sensitivity analyses on the grid cell size were performed, and converged results were obtained. The analytical expressions for oscillating flows in channels with openings were well captured with the numerical solver. Further, the effect of hole size on perforated plates was investigated. Except for an increase in added mass for very small KC numbers, the effect of increasing the hole size (decreasing hole number) on the numerically modeled perforated plates, was, in general, small. The differences were relatively small if using at least three holes on the plate, but using more holes was found numerically favorable due to less stagnation of the flow.

The results from present experimental investigations of two ideal perforated plates of perforations 19 % and 28 % in a two-dimensional setup, are in good agreement with the numerical simulations for oscillating flow in open conditions far from boundaries. The numerical and experimental results demonstrate that the hydrodynamic force on plates of perforation ratios 19-28 % are dominated by damping, with increasing damping dominance for increasing perforation ratio. As an attempt to isolate the effect of plate-end flow separation, channel flow conditions were tested. Although unsuccessful in isolating the plate-end flow separation effect, these trials provided a useful result demonstrating nearly perfect quadratic damping and negligible added mass. The total hydrodynamic force on the plates in channel flow conditions was found to increase considerably compared to open conditions, with increasing difference for increasing amplitude of motion, which can have relevance for, among others, moonpool operations.

The developed solver is two-dimensional, but provided reasonable estimates of the hydrodynamic force coefficients when compared with a previous three-dimensional experimental investigation, despite the fact that the flow separates from four sides in 3D. This could indicate that three-dimensional effects are not dominant for the hydrodynamic forces of perforated plates, and that a two-dimensional viscous flow solver could serve as a tool for estimating hydrodynamic forces on three-dimensional perforated structures. However, the comparison was limited to a three-dimensional experimental investigation of two rectangular perforated plates. These plates had circular holes and perforation ratios of 8 % and 16 %. Further validation, including more perforation ratios and other three-dimensional perforated structures types and shapes, is needed to draw more firm conclusions.

7. Acknowledgement

This work was financed by the Research Council of Norway, NFR project 237929 CRI MOVE.

8. References

[1] F. Mentzoni, M. Abrahamsen-Prsic, T. Kristiansen, Hydrodynamic coefficients of simplified subsea structures, in: ASME 2018 37th International Conference on Ocean, Offshore and Arctic Engineering, 2018.

[2] S. An, O. M. Faltinsen, An experimental and numerical study of heave added mass and damping of horizontally submerged and perforated rectangular plates, Journal of Fluids and Structures 39 (Supplement C) (2013) 87–101.

[3] P. C. Sandvik, F. Solaas, F. G. Nielsen, Hydrodynamic forces on ventilated structures, in: Proceedings of the International Offshore and Polar Engineering Conference, 2006, pp. 54–58.

[4] B. Molin, F. Remy, T. Rippol, Experimental study of the heave added mass and damping of solid and perforated disks close to the free surface, in: Maritime Industry, Ocean Engineering and Coastal Resources - Proceedings of the 12th International Congress of the International Maritime Association of the Mediterranean, IMAM 2007, Vol. 2, 2007, pp. 879–887.

[5] J. Li, S. Liu, M. Zhao, B. Teng, Experimental investigation of the hydrodynamic characteristics of heave plates using forced oscillation, Ocean Engineering 66 (2013) 82 – 91.

[6] B. Molin, Hydrodynamic modeling of perforated structures, Applied Ocean Research 33 (1) (2011) 1–11.

[7] S. An, O. M. Faltinsen, Linear free-surface effects on a horizontally submerged and perforated 2d thin plate in finite and infinite water depths, Applied Ocean Research 37 (2012) 220 – 234.

[8] X. Tian, L. Tao, X. Li, J. Yang, Hydrodynamic coefficients of oscillating flat plates at 0.15 KC 3.15, Journal of Marine Science and Technology 22 (1) (2017) 101–113.

[9] P. Morse, K. Ingard, Theoretical Acoustics, McGraw-Hill, 1968.

[10] O. Faltinsen, A. Timokha, Sloshing, Cambridge University Press, 2009.

[11] A. J. Chorin, Numerical solution of the navier-stokes equations, Mathematics of Computation 22 (104) (1968) 745–762.

[12] P. A. Berthelsen, O. M. Faltinsen, A local directional ghost cell approach for incompressible viscous flow problems with irregular boundaries, Journal of Computational Physics 227 (9) (2008) 4354 – 4397.

[13] H. K. Versteeg, W. Malalasekera, An Introduction to Computational Fluid Dynamics: The Finite Volume Method, Pearson Education Limited, 2007.

[14] S. V. Patankar, Numerical heat transfer and fluid flow, Series on Computational Methods in Mechanics and Thermal Science, Hemisphere Publishing Corporation (CRC Press, Taylor & Francis Group), 1980.

[15] DNV GL AS, Modelling and analysis of marine operations. DNVGL-RP-N103 Edition July 2017, obtained 2017-09-14.

[16] R. Blevins, Applied Fluid Dynamics Handbook, Krieger Pub., 2003.